Phased electromagnetic acoustic transducer array for Rayleigh wave surface defect detection

L. Xiang, D. Greenshields, S. Dixon and R. S. Edwards

***Abstract*—A phased electromagnetic acoustic transducer (EMAT) array system has been developed for detection and characterisation of surface breaking defects. An array of four linear coils which are individually controlled are used to generate a Rayleigh wave. The high current electronics combined with the coil designs enables the array to generate either narrowband or broadband signals, and controlling the phase delay between the channels makes it possible to change the ultrasound wavelength without requiring the physical separation of the coils to be changed. Experimental results show that the four-coil phased array is able to generate a wavelength range from 3.0 mm to 11.7 mm. Surface breaking defects were characterised using a transmit-receive set-up with a broadband EMAT detector being used to detect the Rayleigh wave. Machined surface slots with different depths were used for technique validation. The results show that the array is sensitive to surface defects and that a wide depth sensitivity range for defect sizing can be easily achieved by applying phasing to tune the wavelength of operation. A large increase in detection flexibility is immediately shown.**

***Index Terms*—Rayleigh wave, Phased array, EMAT, Surface Defect Detection**

I. Introduction

Non-destructive testing (NDT) with surface acoustic waves such as Rayleigh waves offers significant benefits for detecting surface cracks. The wave will interact with the crack, with the transmitted and reflected wave properties dependent on the crack geometry and the wavelength and bandwidth of the incident wave [1]. Rayleigh waves have been used for material characterisation [2] and defect sizing [3], [4], [5], [6] for defects on the same side of the sample as the transducers, such as rolling contact fatigue in railways [7], [8] or stress corrosion cracking [9].

Conventional methods of generating Rayleigh waves include using contact piezoelectric transducers with a wedge, or non-contact methods of transduction, such as laser ultrasonics or electromagnetic acoustic transducers (EMATs) [1], [10], [11], [12], [13], [14]. Contact ultrasonic probes require the emitted longitudinal wave to be coupled into the testpiece using couplant, so although these are an accepted and efficient choice, non-contact methods may have advantages as Rayleigh wave generation can be simplified. Laser ultrasound techniques can have adaptable generation using optics [15], [16], but bring safety concerns which can limit applications. EMATs are a viable alternative for Rayleigh wave inspection. An EMAT typically consists of a permanent magnet to introduce a static magnetic field and a coil of wire through which a current is pulsed [17], [18]. By design of the coil and magnet configuration, different wavemode generation can be optimised, and several designs of EMAT have been used for generating Rayleigh waves [8], [18], [12].

All authors are at Department of Physics, University of Warwick, Coventry CV4 7AL, United Kingdom; email r.s.edwards@warwick.ac.uk

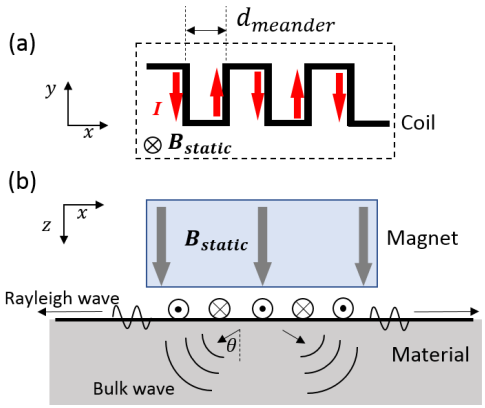

Fig. 1. (a) Birds-eye view of a meander EMAT. (b) A cut-through of (a). Small black arrows in (b) represent the direction of propagation of the sound wave generated by the coil array.

The particle motion for a Rayleigh wave follows an elliptical trajectory, and the wave penetration depth is of the order of a wavelength [19]. Therefore, appropriate selection of the wavelength is critical when using Rayleigh waves to detect or characterise a surface crack. Previous EMAT research has mainly used linear-coil EMATs and has concentrated on low frequency broadband pulses, centred on frequencies around 250 kHz [6], [20], [21].

A linear periodic source pattern can be used to generate a narrowband surface wave signal, for example using lasers and a mask [16], or a meander coil EMAT design. For Lamb waves, selectivity of a wavelength or mode can be controlled by varying the spacing between the source elements [22], [23], [24], [25]. Recent work has optimised the meander coil EMAT design to operate at frequencies of around 2 MHz for Rayleigh waves used to detect shallow defects [12]. Figure 1 shows a schematic diagram of a typical meander EMAT. A permanent magnet is used to introduce the static magnetic field, B_{static}, and the coil is shaped into a meander shape with multiple turns. The current flows through all coil turns simultaneously and the successive turns have an alternating current direction. An approximate relationship between the spacing of the coil turns and the optimal wavelength for generation is given by

$$d_{meander} = (m + \frac{1}{2})\lambda, \tag{1}$$

where $d_{meander}$ is the coil turn spacing, m is an integer, and λ is the ultrasound wavelength, and can be used when designing

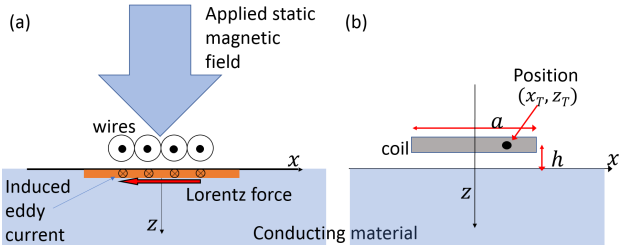

Fig. 2. (a) Schematic diagram of the generation EMAT with a single linear coil. Depths are exaggerated. (b) Model dimensions.

a meander coil for a chosen frequency of operation.

The behaviour of a meander EMAT has been studied by several authors [14], [26], [27]. The use of a single meander EMAT limits inspection to the chosen wavelength defined by equation 1, which can limit the sensitivity to defects. In addition, when operated at high frequency (short wavelength) to detect small defects, the coil dimensions are very small, leading to difficulties in manufacture. Some lift-off from the sample is always required, and the alternating path of the current can cause the dynamic magnetic field to fall off quickly with lift-off for high frequencies. An alternative method which could offer narrowband operation but with a tuneable frequency would bring many benefits in crack characterisation.

This paper proposes an advance in EMAT design, using a phased EMAT array system. A one-dimensional coil array consisting of multiple linear coils is used. The layout of the array is similar to a traditional meander coil design, as shown in figure 1, but each coil (turn) is separate and individually controlled by a multiple-channel driving system. It has been shown in reference [28] that this will give higher amplitude signals. In this paper, we show that different working wavelengths can be selected by delaying the firing time of each coil element. This overcomes the drawbacks of a meander coil design where the fixed bandwidth brings the requirement for multiple EMATs with different coil turn separations.

The paper considers first the Lorentz force generation of a single coil, showing that the phased EMAT array forces can be approximated by a set of rectangular functions for small lift-offs from the sample. The idea behind the phasing and the effective coil turn separation is then introduced, with a spatial impulse model described to explain the frequency behaviour of the array structure, which approximates to equation 1 for large numbers of array elements. The experimental system is then introduced, with a comparison of the output with a set of conventional meander coil EMATs. Finally, the new phased EMAT array is used to characterise a set of slots representing surface-breaking defects, showing the benefits of using multiple wavelengths.

II. Model for the Lorentz Force Generated by a Single Coil

A schematic diagram of a linear coil EMAT is given in figure 2(a). This consists of a series of copper wires wound around a magnet, which is then driven by an alternating current, I. When the coil is placed near a conducting sample, a mirror current, J_y, is induced in the near-surface region [18]. An external static magnetic field, $B_{0,z}$, will give a Lorentz force component

$$F_x = J_y \times B_{0,z} \tag{2}$$

which generates the wave motion. The dynamic field has some effect, but for these EMATs is small compared to the static field, and is not considered here [13]. For a 2D model the induced current J_y can be found by the governing Maxwell equations as [18],

$$J_y = \frac{\partial H_x^M}{\partial z} - \frac{\partial H_z^M}{\partial x}, \tag{3}$$

where H_x^M and H_z^M are the horizontal and vertical magnetic field components within the material near-surface. The latter component is typically neglected. The magnetic field component H_x^M generated by a current through a single wire for unit coil length along the x-axis has been calculated in [18],

$$H_x^M = \frac{\bar{\mu} I}{(1+\bar{\mu})\pi} \frac{h}{h^2 + x^2} e^{\frac{-(1+i)z}{\delta}} \tag{4}$$

where h is the vertical distance between the coil and the material surface, δ is the electromagnetic skin depth given by $\sqrt{2/\omega\sigma\mu_0\bar{\mu}}$, ω is the angular frequency, σ and μ_0 are the free-space electrical conductivity and permeability and $\bar{\mu}$ is the material relative permeability.

A linear coil has multiple turns and therefore a finite width which must be considered when analysing the force generated. A coil of width a, existing at positions (x_T, z_T) from $(-a/2, -h)$ to $(+a/2, -h)$, can be approximated as a very thin sheet of current of width a, as shown in figure 2(b). The spatial distribution of the total magnetic field is then

$$\begin{aligned} H_x^M(x,z) &= \frac{\bar{\mu} I}{(1+\bar{\mu})\pi} e^{\frac{-(1+i)z}{\delta}} \int_{-a/2}^{a/2} \frac{h \, dx_T}{h^2 + (x - x_T)^2} \\ &= \frac{\bar{\mu} I}{(1+\bar{\mu})\pi} e^{\frac{-(1+i)z}{\delta}} \times \\ &\quad \left[\arctan\left(\frac{x + a/2}{h}\right) - \arctan\left(\frac{x - a/2}{h}\right) \right]. \end{aligned} \tag{5}$$

Substituting this into equation 3 gives

$$J_y(x,z) \approx \frac{\partial H_x^M(x,z)}{\partial z} = -\frac{(1+i)}{\delta} H_x^M(x,z). \tag{6}$$

The resulting Lorentz force is approximated as a surface force, as the skin depth in a metal is small.

The profile of the force generated shows a dependence on the lift-off h via these equations. Figure 3 shows calculation of the normalised Lorentz force profile for a set of lift-off values for $a = 1.5$ mm. As the lift-off approaches zero, the force can be approximated as a square wave with width a. For practical experiments the lift-off of the EMATs is kept to a minimum to ensure optimum signal to noise, and therefore for the rest of this paper, the coil will be approximated as a thin sheet with very small lift-off, giving a normalised Lorentz force for each coil (assuming the static field dominates) of

$$F_x = \begin{cases} 1 & |x| \leq a/2, \\ 0 & \text{otherwise.} \end{cases} \tag{7}$$

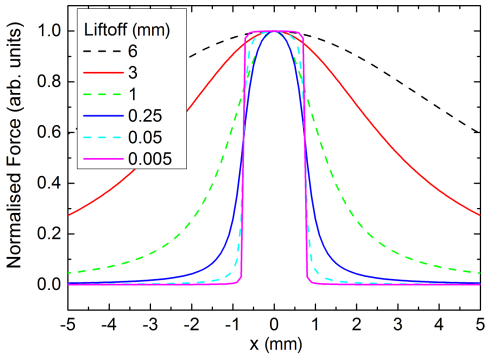

Fig. 3. Calculation of the normalised Lorentz force profile for different lift-offs.

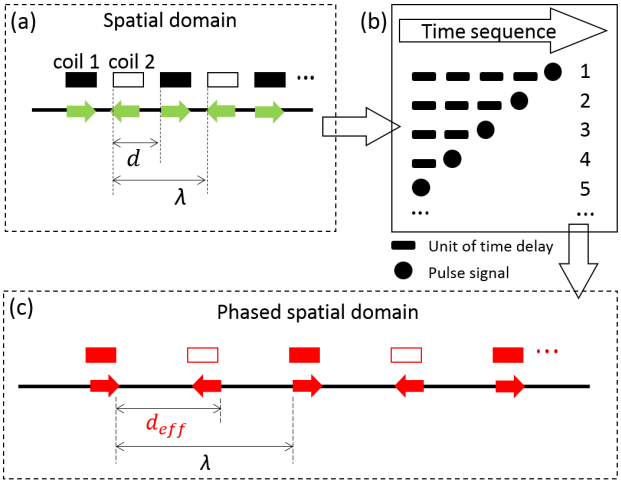

Fig. 4. The modality of the phased EMAT array. (a) shows the physical separation of the coils; (b) shows the delay (dash) and pulse time (spot) of each channel; (c) shows the effective separation obtained by the delay process.

III. Phased Array EMAT for Rayleigh Wave Generation: Calculations

A coil array is described and modelled here for generating narrowband Rayleigh waves with a choice of central wavelength. A set of linear coils with fixed spacing is used as the array elements.

A. Phased spatial domain

Figure 4(a) shows a schematic diagram of the physical array of linear EMAT coils. The coils are separated by a fixed physical separation d, with alternating polarity of the current through each coil (shown by the colour). This leads to a designed wavelength λ, described by equation 1 for many elements, with a central frequency $f_p^* = c_R/\lambda$ for a Rayleigh wave velocity c_R. The linear coils are assumed to be long compared to their separation and their width, to allow approximation in two-dimensions.

The phased electronic current driver system allows the coils to be activated sequentially, as shown in figure 4(b). For example, coil 1 could be activated at time $t = 0$, coil 2 at time t, coil 3 at a time $2t$, etc. The surface waves generated by coil 1 would then have moved closer to coil 2 before it is activated, making the separation of the coils appear to be

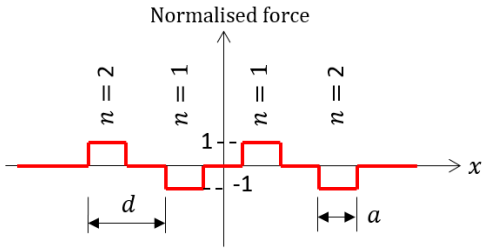

Fig. 5. Normalised force profile for two pairs of coils. The force for each coil is described by equation 7, and the current is taken to be passing through each coil in alternating directions. This forms the spatial model of the EMAT Lorentz force array.

smaller for waves travelling to the right. Conversely, for N' coils, coil N' could be activated at time $t = 0$, coil $N' - 1$ at time t, coil $N' - 2$ at time $2t$... For this configuration, shown in figures 4(b)&(c), the wave from coil N' would travel a set distance before coil $N' - 1$ is activated, making the separation between the coils appear larger.

By this phasing process, an effective separation between coils d_{eff} can be defined. The designed wavelength of the system is then $\lambda = 2d_{eff}$. The time delay factor for element j to choose an effective separation is

$$\Delta\tau = j\frac{d - d_{eff}}{c_R}. \tag{8}$$

B. The spatial impulse response

The simple equations described above can be used as a rough guide for designing a phased EMAT array which operates in a similar manner to a meander coil design. Ideally, constructive interference would be obtained by a point source array. However, for a surface wave EMAT the coil elements are of finite size, due to the inefficient nature of the coupling mechanism. The frequency content of any generated Rayleigh waves will depend on the effective coil separation, the driving current frequency, the number of coils, and the coil width. Very narrow width coils could be used to allow high frequency operation, but this generally leads to fewer coil turns, a lower induced current density, and therefore a small signal to noise ratio. This section analyses the spatial behaviour of the proposed array when an arbitrary geometry is defined, calculating the interaction between the array parameters and the limits on the wavelengths that can be generated.

Several models have been investigated to predict the Rayleigh wave frequency behaviour for a linear or racetrack EMAT [13], [28], [29]. Where a broadband detector is used, the generated surface wave properties show a convolution relation between the input temporal function and the spatial profile of the generating source. Thus, a simple model of the Lorentz force induced by the coil array is presented here and analysed to understand the array spatial behaviour, building on the approximation of the Lorentz force as a rectangular function of width a for small lift-off from the sample. The

array of linear coils can be described by

$$f_x(x) = \sum_{n=1}^{N}(-1)^n \times \left[\text{rect}\left(\frac{x-(n-\frac{1}{2})d}{a}\right) - \text{rect}\left(\frac{x+(n-\frac{1}{2})d}{a}\right)\right]$$
$$\text{where} \quad \text{rect}(u) = \begin{cases} 1 & |u| \leq \frac{1}{2}, \\ 0 & \text{otherwise}, \end{cases} \tag{9}$$

where N indicates the total number of coil dipoles, i.e. number of pairs of coils with alternating current directions, and n denotes which pair is being considered. A schematic diagram of the normalised force generated by this array is given in figure 5 for $N = 2$, i.e. two pairs of coils, for current passing through the coils in alternating directions to match the design of a meander coil.

The structural response of the coils can be calculated by taking the Fourier transform of $f_x(x)$,

$$\begin{aligned}\hat{f}_x(k) &= \int_{-\infty}^{\infty} f_x(x)e^{-ikx}dx \\ &= -4di\sin(\frac{1}{2}ka)\times \\ &\quad \sum_{n=1}^{N}(-1)^n\{(n-\frac{1}{2})\,\text{sinc}[(n-\frac{1}{2})kd]\},\end{aligned} \tag{10}$$

where $k = 2\pi/\lambda$ is the wavenumber. It can be seen from equation 10 that the response of the array spatial model has a functional dependence on both a, d and N. In practice, ultrasound generation is defined by the temporal frequency f, and for the non-dispersive Rayleigh wave the Fourier transform can simply be updated using $k = 2\pi f/c_R$, giving

$$g(f) = -2di\sin(\frac{\pi a}{c_R}f)\sum_{n=1}^{N}\{(-1)^n(2n-1)\,\text{sinc}[(2n-1)\frac{\pi d}{c_R}f]\}. \tag{11}$$

The modulus of this is used to define the frequency behaviour $T(f)$. The terms in $g(f)$ can be separated,

$$\begin{aligned} &T(f) = \alpha(d)D(f,a)H(f,d,N), \\ &\text{where } \alpha = 2d, \\ &D(f,a) = |\sin(\frac{\pi a}{c_R}f)|, \\ &H(f,d,N) = |\sum_{n=1}^{N}\{(-1)^n(2n-1)\,\text{sinc}[(2n-1)\frac{\pi d}{c_R}f]|. \end{aligned} \tag{12}$$

α is a separation-dependent coefficient, and $D(f,a)$ is defined as the spatial response of a coil of width a. $H(f,d,N)$ is the spatial response of the layout of the coil array, and depends on frequency, coil separation and the number of coil pairs, and recreates the behaviour of a meander coil.

$D(f,a)$ and $H(f,d,N)$ both exhibit periodicity. For $D(f,a)$, the spatial period is c_R/a, and the frequencies that provide greatest magnitude response appear at $f_p^D = (2m+1)c_R/2a$, where m is zero or an integer. This is shown in figure 6(a). For $H(f,d,N)$, the periodicity depends on both d and N, with calculations shown in figure 6(b)-(e) for different values of N and a fixed d. As N is increased, the peaks become sharper and the first non-zero frequency peak approaches the predicted meander coil operational frequency given by equation 1, and $f_p^H = c_R/2d$.

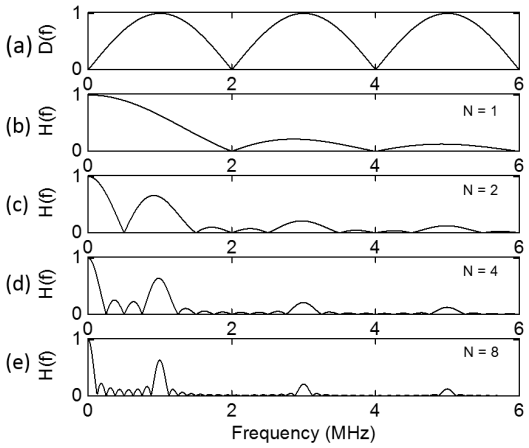

Fig. 6. Example $D(f,a)$ and $H(f,d,N)$ for $d = a = 1.5$ mm and velocity $c_R = 3000$ m/s. $H(f,d,N)$ is shown for N =1, 2, 4 and 8.

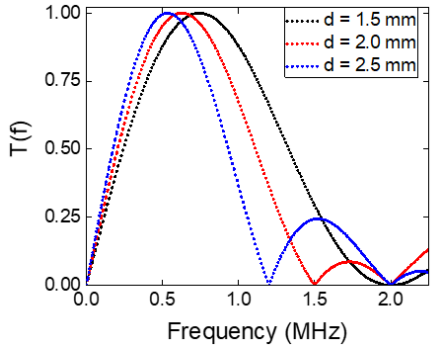

Fig. 7. The full response when $N = 1$, $c_R = 3000$ m/s and a is fixed at 1.5 mm. Three lines indicates $T(f)$ when d is 1.5 mm, 2.0 mm and 2.5 mm.

The full frequency response T depends on the product of $D(f,a)$ and $H(f,d,N)$, and will give a peak magnitude response at a frequency f_p^T. The behaviour splits into three regimes which depend on the geometry of the array: $d > a$, $d = a$, and $d < a$. For $d > a$ and $N \geq 2$ the behaviour matches that of a conventional meander coil, with the frequency behaviour dominated by the sharp peaks in $H(f,d,N)$, approaching $f_p^* = c_R/2d$ for large N.

For $N = 1$ the system has a single pair of coils, and the peak behaviour is shown in figure 7. The limit on the geometry is where $d = a$, and there is no space between a coil and its neighbour. Here, the $N = 1$ system recreates a racetrack coil. For a pair of coils with $a = 0.75$ mm, $f_p^T = 0.761c_R/2d$, from the product of $D(f,a)$ and $H(f,d,N)$, confirming the square wave model for a racetrack coil from reference [29]. The regime where $d < a$ is not practical for a standard meander coil design, as the turns are then overlapping.

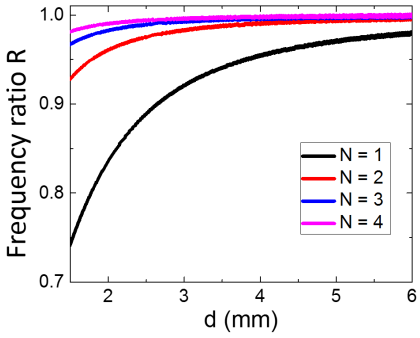

Fig. 8. Behaviour of the ratio of the frequency generated to that designed (equation 13) as a function of coil separation d for $a = 1.5$ mm, and d varied between 1.5 mm and 6.0 mm.

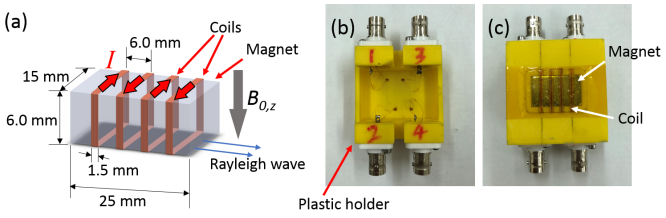

Fig. 9. Schematic of the Rayleigh wave array EMAT. Parameters of the array are: $a = 1.5$ mm, $d = 6.0$ mm and the number of coil dipoles $N = 2$. (a) Configuration of the coils and the permanent magnet. The 3D printed transducer holder from (b) the front and (c) back.

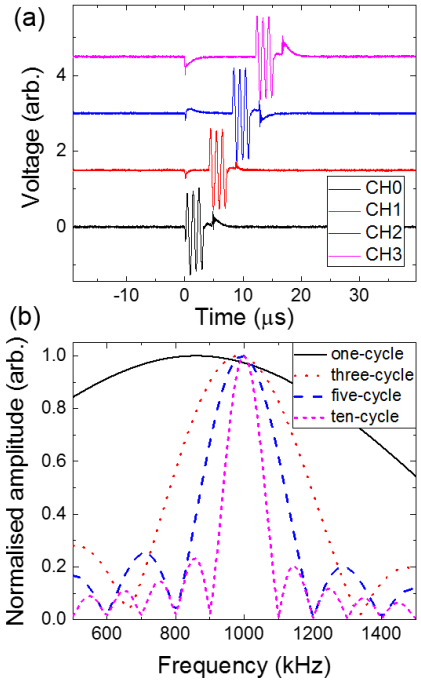

Fig. 10. The driving signal at 1 MHz, showing (a) the output of each channel for three-cycle operation, and (b) frequency information.

A dimensionless quality R is defined as

$$R(d) = \frac{f_p^T(d)}{f_p^*(d)}, \tag{13}$$

where f_p^T is numerically solved from equation 12 for a chosen a, with results shown in figure 8 for $a = 1.5$ mm with d increasing from 1.5 to 6.0 mm. f_p^T approaches f_p^* when $d \gg a$, i.e. when the desired wavelength is much larger than the element width, each coil can be approximated as a point source. However, when d becomes comparable to a, the drop of f_p^T is obvious and the influence of the coil width can no longer be neglected. In addition, a large N can lead to a higher f_p^T when d and a are closer together in size.

The rule of thumb for meander coils described by equation 1 will hold for large N and for $d \gg a$, while for smaller N or as $d \to a$ the frequency will be reduced. This calculation will hold for a conventional meander coil design with fixed d, but will also hold for the effective separation d_{eff} obtained using phasing, with d replaced by d_{eff} throughout.

IV. Phased Array EMAT for Rayleigh Wave Generation: Experiments

A. Experimental details

To validate the concept, a four-coil ($N = 2$) transducer prototype was built. The 3-D sketch of the EMAT is shown in figure 9(a). A permanent NdFeB block magnet of dimensions $25 \times 15 \times 6$ mm was used to introduce the static magnetic field. Copper wires were tightly wrapped onto the magnet to produce four identical coils, each with seven turns of 0.2 mm diameter copper wire and a total coil width of 1.5 mm including spacing. The physical separation between the coils was fixed at $d = 6.0$ mm, with the variation of the static magnetic field over this range minimal. Figures 9(b)&(c) show photographs of the transducer in a 3D-printed case.

A four-channel high energy pulser was used to drive the EMAT array. The pulser was custom-made based on FPGA modules, with the capability to deliver controllable sinusoidal bursts. This gives a lower output voltage than the pulsed phase array controller reported in [30], but allows longer bursts. The duration of the burst signals can be varied from one-cycle to ten-cycles and the centre frequency can be from 10 kHz to 10 MHz. The four channels can be individually controlled and give a maximum current output of about 70 A. The firing delay between channels can be set from 0 to 10 s, in 5 ns steps. Figure 10(a) shows the voltage outputs from all four channels for a 1 MHz three-cycle driving signal, with a time delay between the successive channels of 4 μs. Figure 10(b) shows the magnitude frequency spectrum of the signals generated from one of the channels for different numbers of cycles, showing broadband (one cycle) or narrowband driving.

A broadband racetrack EMAT detector was used to receive the generated Rayleigh wave signal, with a total width of 3 mm, length of 25 mm, and using an identical magnet to the generation EMAT. The sensitivity range of the detector was between 0 and 4 MHz, dependent on the coil width [29]. The received signal was passed through an amplifier and a 2.5 MHz low pass filter before being recorded by a digital oscilloscope. The separation between the generation array and detection EMAT was set to 100 mm for all experiments. Analysis of the frequency behaviour used an 85 mm thick aluminium bar, while crack detection used a 60 mm thick aluminium bar containing several machined slots. The set-up is shown in

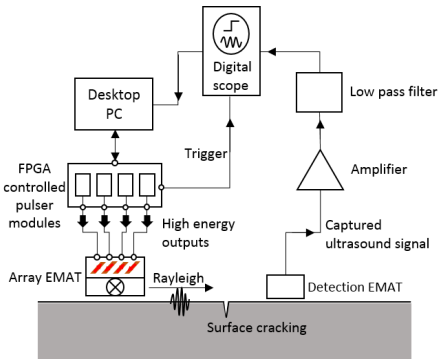

Fig. 11. Diagram showing the experimental set-up.

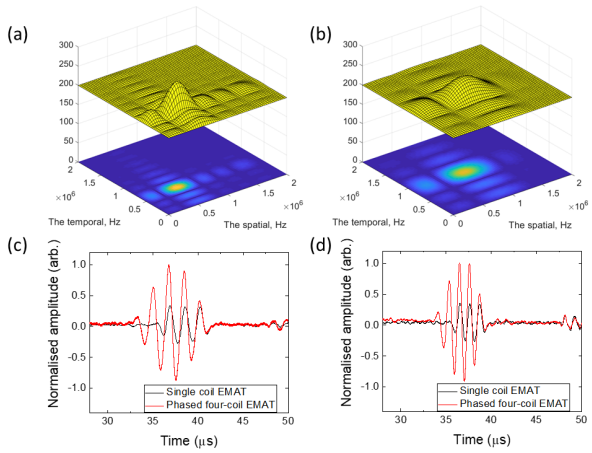

Fig. 12. Generation of Rayleigh waves for wavelengths 3.06 mm and 4.84 mm. (a) and (b) show the calculated frequency spectra for the temporal driving signals and the spatial responses from the array structure. (c) and (d) are the experimental Rayleigh signals. (a) and (c) are for $\lambda = 3.06$ mm and a centre frequency of the driving signal of $f_0 = 950$ kHz for $d_{eff} = 1.5$ mm. (b) and (d) are for $\lambda = 4.84$ mm, $f_0 = 600$ kHz and $d_{eff} = 2.40$ mm.

figure 11 for where there is a slot present.

B. Four-coil phased operation

1) Enhanced signal amplitude & geometry dependence: Sequentially delaying the firing time of the EMAT coils allows one to overlap the Rayleigh wave generated from every element, such that an increased signal amplitude can be obtained [28]. The time delay factor for the jth coil element is $\Delta\tau_j = d_{j,0}/c_R$, where $d_{j,0}$ is the physical separation between the jth element and the reference element.

A convolution of the two domains (spatial and temporal) give the final resulting Rayleigh wave. The behaviour must be calibrated such that the desired wavelength (or frequency) can be generated. When using the four channel pulser to drive the four-coil prototype, a three-cycle burst was normally chosen such that the signal was narrowband but also provided good resolution in the time domain. Two examples are given to show the behaviour in figure 12 for two different designed wavelengths. (a) and (b) show the result of calculations of the magnitude response in the Fourier domain, for variation of the driving frequency (temporal axis) and from the spatial response of the chosen geometry (spatial axis). Both predict a peak around the designed frequency. (c) and (d) show the experimental results, with the comparison of the output signals from a single coil and four-coil operation, showing the expected increase in signal. Note that the same 3-cycle pulse was used for all measurements. When the phase delays are used to obtain different values for d_{eff}, the overlap and time shifting leads to an small apparent increase in cycles. Ideally, the EMAT coils would have a single turn such that the sources for constructive interference are close to line sources. However, practically the EMAT coils must have finite width due to efficiency limitations, but reasonable constructive interference can still be obtained, as described in section III-B.

2) Comparison with a conventional meander coil: The EMAT shown in figure 9 with a fixed separation was used with the phased pulser to mimic a set of conventional meander coil designs which were produced. These all contained four meander turns with separations of 2.4, 3.6 or 4.8 mm, a coil width of 1.5 mm and length of 20 mm, with the designs shown in the insets of figure 13, and the same magnet as for the phased EMAT array. The conventional meander EMATs were driven by a single channel of the pulser and comparisons were made with the phased EMAT array when the pulser was set to give a matched value of d_{eff}. The centre frequency of the driving signal was progressively increased from 200 kHz to 2.0 MHz, with a 100 kHz step and 32 signals were averaged to eliminate the incoherent noise. The peak-peak amplitude of the detected Rayleigh wave was recorded at each frequency. and is plotted in figure 13.

The behaviour of the conventional meander and the phased EMAT array match well, with minor differences due to impedance of lift-off variations during the experiments. The second harmonic becomes obvious when the coil separation increases, as shown in figure 13(b) and (c). This can be mathematically understood from the coil array structural response discussed earlier or from constructive interference of the waves. The behaviour of the detector as a velocity sensor will also dominate when considering which frequencies the system will detect more strongly.

3) Selectivity of wavelength: The convolution between the driving temporal domain and the phased spatial domain allows one to generate multiple wavelengths of Rayleigh wave through variation of d_{eff} and the central driving frequency f_0. The effective separation, d_{eff}, of the four-coil array was varied from 6.0 mm (physical separation) to 1.0 mm (regime where $d_{eff} < a$) with a 0.25 mm step. The centre frequency f_0 of the driving signal at each d_{eff} was varied between 200 kHz and 1.5 MHz, with a 25 kHz step and a three-cycle duration. The detected signal was recorded and the peak-peak value was found to represent the efficiency when the phased array was in the corresponding $(d_{eff},\ f_0)$ setting. Results are presented in figure 14, showing the main wavelength obtained for each d_{eff}. Also shown is the rule of thumb prediction, where $\lambda = 2d_{eff}$.

The results are closer to the prediction as N increases, as expected. The behaviour is also closer to the predicted behaviour when d_{eff} is larger than a. The upturn in the results at low values of d_{eff} indicates that the width of the coil is beginning to dominate the obtained frequency behaviour, as

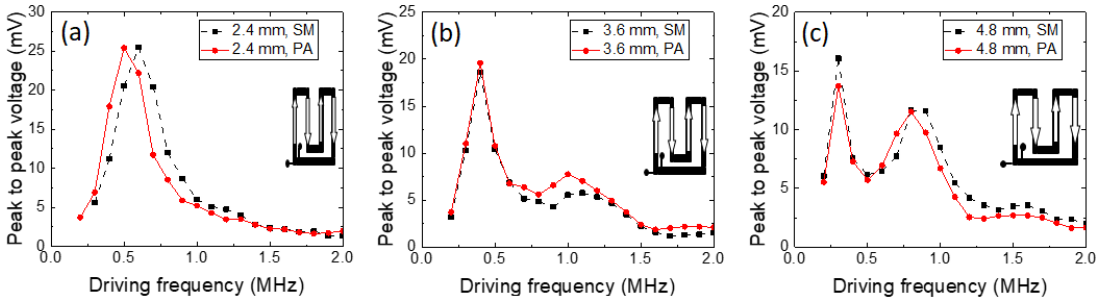

Fig. 13. Comparisons of the frequency behaviour between a conventional, or standard, meander (SM) and the four-coil phased array (PA) EMAT, for d or d_{eff} of (a) 2.4, (b) 3.6 and (c) 4.8 mm. The coil geometry of the SM EMAT is given in the insert.

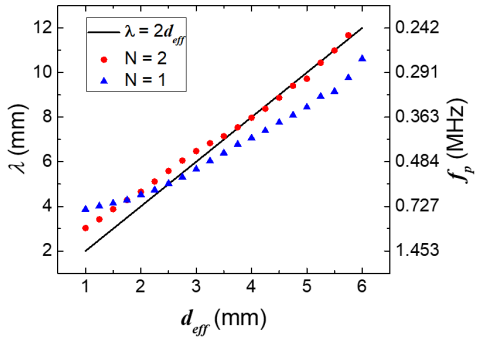

Fig. 14. The generated wavelength for a chosen d_{eff}, for activation of one or two dipole pairs of coils. Higher N gives closer to the predicted behaviour shown by the straight line.

predicted by the equations presented in section 3.

V. Measurement of Surface Breaking Defects

The ability to use the proposed phased EMAT array to detect surface cracks was validated by scanning an aluminium sample containing three machined vertical surface slots. All slots were vertical and their width was 1.0 mm. The slot depths were A:1.0, B:2.5 and C:5.0 mm. The effective separation and driving centre frequency setting of the array was set following the optimised results given in figure 14. For example, to generate a Rayleigh wave with a wavelength 5.59 mm, the $(d_{eff},\ f_0)$ for the array was (2.5 mm, 0.52 MHz).

A. Defect detection

Figure 15 shows the behaviour for $\lambda = 5.59$ mm, for a clean surface (black dashed lines) and for two different depth defects (red lines). For the shallow 1 mm depth crack, the Rayleigh wave amplitude dropped by only a small amount as most of the wave energy was transmitted underneath the crack. For the 5 mm deep crack, the majority of the energy was blocked by the crack and only a small amplitude signal was recorded. This demonstrates that a higher sensitivity to small cracks can be obtained by generating a smaller wavelength.

B. Depth gauging

The tuneability of the Rayleigh wavelength offers a unique ability to analyse crack geometry. For example, a small wavelength could be used when scanning a sample, which would

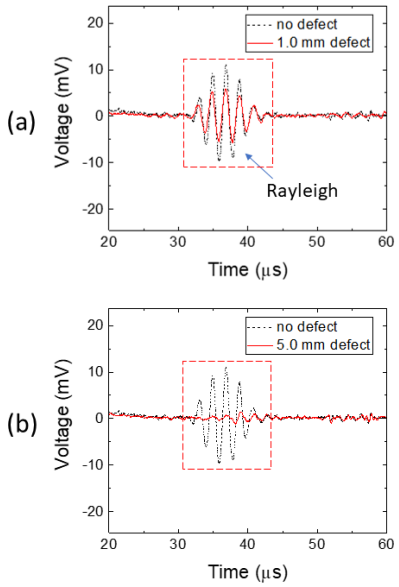

Fig. 15. Crack sensing by the four-coil phased array for $d_{eff} = 2.5$ mm and $f_0 = 0.52$ MHz, and a generated wavelength of 5.59 mm. Two A-scans obtained for cracks A and C.

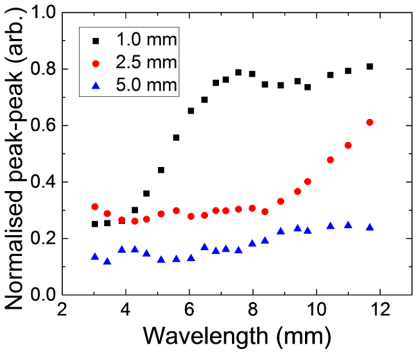

Fig. 16. Results of measuring the surface defects by the phased array EMAT. Different wavelengths were sent and the wave transmission coefficient was recorded.

offer primarily a *yes/no* answer as to whether a crack was present without sizing information. Once a crack was identified, the depth could be gauged by varying the wavelength and identifying the cut-off frequency of the crack.

Figure 16 shows the output of such a measurement for three different depth defects. For each defect, the effective

separation d_{eff} and hence wavelength were varied with the generation and detection EMATs at fixed positions on either side of the defect, and the peak-peak transmitted amplitude of the wave was plotted as a function of wavelength. Normalisation was done in comparison with the 'no defect' measurement, indicating that some energy is still blocked even for larger wavelengths, as expected [3]. For the 1 mm deep slot the filtering behaviour can be clearly seen, with longer wavelengths mainly able to pass underneath the crack and short wavelengths mostly blocked. The 2.5 mm slot shows the start of the transition to waves being able to pass underneath the slot for higher wavelengths. The 5 mm deep slot predominantly blocked signals over all wavelengths investigated, as expected; even for a 10 mm wavelength, the crack depth is still significant compared to the wavelength and will block a significant amount of the wave energy. Some amplitude is measured even for small wavelengths, where Rayleigh waves should be blocked, due to a mode-converted longitudinal to shear (and vice-versa) wave which arrived close to the Rayleigh wave arrival time. The amplitude of this wave varied with d_{eff} due to interference effects, with the amplitude strongest for short wavelengths. In addition, for the 1 and 2.5 mm deep slots the scans were made close to the sample edge due to the presence of deep slots on the side face, adding the effect of edge reflections.

From the above work, two things are of note. Firstly, the in-house built phased array EMAT system shows a good sensitivity for detecting surface cracks over a wide range of depths. For shallower cracks waves will be transmitted, but the blocking of the wave becomes very clear when a smaller wavelength is used. Secondly, to widen the depth monitoring range, one can expand the range of λ. For example, to characterise a 2.5 mm deep crack, a maximum wavelength greater than 12 mm should be used. Since sub-mm cracks offer uncertain hazards and challenges for detection, smaller wavelengths are needed and can be generated from changing the phased array parameters and producing narrower coils.

VI. Conclusion

A Rayleigh wave phased EMAT array system for detecting surface breaking defects has been proposed. A one-dimensional linear coil array was formed to generate Rayleigh waves, with the neighbouring coils having opposing polarisation of the current. Constructive interference of the Rayleigh wave is obtained by delaying the pulses from each channel, and matching the phase difference between the coils. A four-channel high energy pulser was built to drive the four-coil EMAT array. By phasing each coil element individually and adjusting the driving signal, multi-wavelength generation is possible, using a single EMAT array with fixed spacing. A large enhancement of detection possibility can be obtained by applying the proposed phased array to samples, offering not only an improvement in signal to noise ratio when compared to a conventional single linear coil EMAT, but also the full control of the ultrasound waveform with either broadband or narrowband operation with different centre frequencies.

The system was used to detect surface slots, showing sensitivity to defects as small as 1 mm deep, with smaller depths possible but not tested. To build an array with a higher sensitivity to smaller defects further optimisation is needed. Discussion of the spatial behaviour of the array pattern given in the paper will aid in design of a new array, by offering the ability to calculate the frequency response for different coil widths and effective spacings. The bandwidth limit due to the finite width of each coil element cannot be neglected when one is aiming for high frequency or small wavelength operation. Increasing the number of coils can compensate for the frequency reduction that is caused by the coil finite size; an array with a larger number of activated coils will offer a better spatial filter than one with fewer active coils.

The generation-detection configuration used in this paper shows great potential for fast on-line scanning over a large area. However, one could further improve the efficiency of testing by extending this to a 2D scan, such that the scan could be done over the finite length of the cracks.

References

[1] I. A. Viktorov, Rayleigh and Lamb Waves: Physical Theory and Applications, 1967.

[2] M. Duquennoy, M. Ouaftouh, M. Ourak, Ultrasonic evaluation of stressed in orthotropic materials using Rayleigh waves, NDT&E International 32 (1999) 189–199.

[3] R. S. Edwards, S. Dixon, X. Jian, Depth gauging of defects using low frequency wideband Rayleigh waves, Ultrasonics 44 (2006) 93–98.

[4] D. G. Aggelis, T. Shiotani, D. Polyzos, Characterization of surface crack depth and repair evaluation using Rayleigh waves, Cemant&Concret Composites 31 (2009) 77–83.

[5] J. A. Cooper, R. A. Crosbie, R. J. Dewhurst, A. W. McKIE, S. B. Palmer, Surface acoustic wave interations with cracks and slots: A noncontacting study using lasers, IEEE Trans Ultrason Ferroelectr Freq Control 33 (1986) 462–70.

[6] X. Jian, S. Dixon, N. Guo, R. Edwards, Rayleigh wave interaction with surface-breaking cracks, Journal of Applied Physics 101 (2007) 064906.

[7] R. E. Schramm, P. J. Shull, A. V. Clark, Jr., D. V. Mitrakovic, EMATs for roll-by crack inspection of railroad wheels, Review of Progress in Quantitative Nondestructive Evaluation 8 (1989) 1083–1089.

[8] R. S. Edwards, S. Dixon, X. Jian, Characterisation of defects in the railhead using ultrasonic surface waves, NDT & E International 39 (2006) 468–475.

[9] F. Hernandez-Valle, A. R. Clough, R. S. Edwards, Stress corrosion cracking detection using non-contact ultrasonic techniques, Corrosion Science 78 (2014) 335–342.

[10] F. Hernandez-Valle, B. Dutton, R. S. Edwards, Laser ultrasonic characterisation of branched surface-breaking defects, NDT & E International 68 (2014) 113–119.

[11] S. Dixon, S. E. Burrows, B. Dutton, Y. Fan, Detection of cracks in metal sheets using pulsed laser generated ultrasound and EMAT detection, Ultrasonics 51 (2011) 7–16.

[12] C. B. Thring, Y. Fan, R. S. Edwards, Focused Rayleigh wave EMAT for characterisation of surface-breaking defects, NDT &E International 81 (2016) 20–27.

[13] X. Jian, S. Dixon, K. T. V. Grattan, R. S. Edwards, A model for pulsed Rayleigh wave and optimal EMAT design, Sensors & Actuators A 128 (2006) 296–304.

[14] S. Wang, R. Su, X. Chen, L. Kang, G. Zhai, Numerical and experimental analysis of unidirectional meander-line coil electromagnetic acoustic transducers, IEEE Transducers on Ultrasonics, Ferroelectrics, and Frequency Control 60 (2013) 2657.

[15] D. A. Hutchins, Ultrasonic generation by pulsed lasers, Physical Acoustics 18 (1988) 21–123.

[16] T. Stratoudaki, J. A. Hernandez, M. Clark, M. G. Somekh, Cheap optical transducers (CHOTs) for narrowband ultrasonic applications, Measurement Science and Technology 18(3) (2007) 843–851.

[17] R. B. Thompson, Physical principles of measurement with EMAT transducers, Physical Acoustics 19 (1990) 157–200.

[18] M. Hirao, H. Ogi, Electromagnetic Acoustic Transducers: Noncontacting Ultrasonic Measurements using EMATs, Springer, 2017.

[19] J. L. Rose, Ultrasonic Guided Waves in Solid Media, Cambridge University Press, 2014.
[20] R. S. Edwards, B. Dutton, A. R. Clough, M. H. Rosli, Enhancement of ultrasonic surface waves at wedge tips and angled defects, Applied Physics Letter 99 (2011) 094104.
[21] M. H. Rosli, R. S. Edwards, Y. Fan, In-plane and out-of-plane measurements of Rayleigh waves using EMATs for characterising surface cracks, NDT & E International 49 (2012) 1–9.
[22] R. C. Addison, A. D. McKie, Generation and detection of single mode Lamb waves using laser-based ultrasound, Review of Progress in Quantitative Nondestructive Evaluation 14 (1995) 521–528.
[23] R. S. C. Monkhouse, P. D. Wilcox, P. Cawley, Flexible interdigital PVDF transducers for the generation of lamb waves in structures, Ultrasonics 35 (1997) 489–498.
[24] J. L. Rose, S. P. Pelts, M. J. Quarry, A comb transducer model for guided wave NDE, Ultrasonics 36 (1998) 163–169.
[25] W. Zhu, J. L. Rose, Lamb wave generation and reception with time-delay periodic linear arrays: a BEM simulation and experimental study, IEEE Transactions on ultrasonics, ferroelectrics, and frequency control 46 (1999) 654–664.
[26] H. Talaat, E. Burstein, Phase-matched electromagnetic generation and detection of surface elastic waves on nonconducting solids, Jounal of Applied Physics 45 (1974) 4360.
[27] Y. Xie, Z. Liu, L. Yin, J. Wu, P. Deng, W. Yin, Directivity analysis of meander-line-coil EMATs with a wholly analytical method, Ultrasonics 73 (2017) 262–270.
[28] J. Tkocz, S. Dixon, Electromagnetic acoustic transducer optimisation for surface wave applications, NDT&E International 107 (2019) 102142.
[29] C. B. Thring, S. J. Hill, S. Dixon, R. S. Edwards, The effect of EMAT coil geometry on the Rayleigh wave frequency behaviour, Ultrasonics 99 (2019) 105945.
[30] J. Tkocz, D. Greenshields, S. Dixon, High power phased EMAT arrays for nondestructive testing of as-cast steel, NDT&E International 102 (2019) 47–55.